

Pattern recognition with superconducting wirelet neurons

Khalil Harrabi^{1,2}, Leonardo R. Cadorim³ & Milorad V. Milošević³

¹*Physics Department, King Fahd University of Petroleum and Minerals (KFUPM), 31261 Dhahran, Saudi Arabia*

²*Interdisciplinary Research Center for Advanced Quantum Computing, King Fahd University of Petroleum and Minerals (KFUPM), 31261 Dhahran, Saudi Arabia*

³*COMMIT, Department of Physics, University of Antwerp, Groenenborgerlaan 171, B-2020 Antwerp, Belgium*

Neuromorphic computing aims to reproduce the energy efficiency and adaptability of biological intelligence in hardware. Superconducting devices are an attractive platform due to their ultra-low dissipation and fast switching dynamics. Here we introduce a shunted superconducting wirelet as an artificial neuron, representing the simplest possible superconducting neuron implementation. This minimal design, a single superconducting channel with a resistive shunt, enables straightforward fabrication, electronic control, and high scalability. The neuron exhibits spiking voltage behavior driven by the interplay of resistive switching and relaxation, with key properties such as threshold, firing frequency, and refractory time tunable via applied current, temperature, and shunt resistance. We further show that the resulting temporal voltage signals can be incorporated into a training algorithm to achieve accurate pattern recognition, demonstrating suitability for neuromorphic tasks. Finally, we discuss on-chip training using similar wirelets with gated synaptic weights, establishing a scalable,

energy-efficient building block for cryogenic artificial intelligence hardware, integrable with other emergent superconducting technologies.

Superconducting neurons are engineered to replicate the functionality of biological neurons using superconducting materials and circuits. These artificial neurons exhibit key functional attributes including spiking behavior, synaptic connectivity, and signal processing capabilities, which are essential for developing neuromorphic systems that emulate the brain's information-processing abilities. Central to their functionality is the ability to generate and propagate spikes, similar to action potentials in biological neurons. In biological systems, neurons communicate via electrical spikes transmitted across synapses, leading to activation or inhibition of other neurons within a network. Superconducting neurons replicate this behavior using Josephson junctions, superconducting devices that easily switch between states in response to input current signals and can be configured to produce discrete voltage pulses analogous to biological spikes. The pulses propagate through superconducting circuits with minimal energy loss, enabling ultra-fast and efficient signal transmission. Spiking dynamics can be tuned by adjusting parameters such as critical current and junction capacitance, allowing precise control over neuronal behavior^{1,2}. Beyond spike generation, superconducting neurons must establish synaptic connections to form functional networks. In biological systems, synapses transmit signals between neurons and play a central role in learning and memory by modulating connection strength. In superconducting systems, synaptic functionality can also be implemented using Josephson junctions or related superconducting elements. These artificial synapses are engineered to modulate signal strength and timing, mimicking biological plasticity. For example, synaptic weight may be adjusted by varying current or magnetic flux ap-

plied to a Josephson junction, enabling adaptive learning based on input signals. This tunability is fundamental for neuromorphic systems performing learning and memory tasks^{3,4}. Superconducting neurons are also capable of sophisticated signal processing required for complex computation. Within a network, each neuron integrates multiple input signals, processes them according to its internal state, and generates an output spike when a threshold is reached. This mirrors the integrate-and-fire model of biological neurons, where inputs are summed and an action potential is triggered once the membrane potential exceeds threshold. The intrinsic high-speed operation of superconducting circuits enables signal processing at extremely fast rates, which is essential for real-time applications such as artificial intelligence and quantum computing. Superconducting neurons can also be coupled with superconducting qubits in quantum processors, enabling hybrid architectures that combine neuromorphic and quantum computing advantages. Additionally, the low energy dissipation of superconducting circuits allows such computations to be performed with minimal power consumption, supporting large-scale network integration⁵.

Despite these advantages, superconducting neurons based on Josephson junctions exhibit substantial complexity. Circuit architectures such as single-flux quantum (SFQ) and adiabatic quantum-flux-parametron (AQFP) systems are commonly employed to implement neuronal functions including integration, inhibition, and temporal summation. However, these architectures require precise biasing schemes and accurate magnetic flux control to prevent cross-talk and unintended coupling between neighboring elements. Implementing synaptic plasticity introduces additional challenges. Superconducting synapses typically rely on Josephson junctions or hybrid elements that modulate synaptic weight through controlled magnetic fields or current biases, neces-

sitating careful calibration and external feedback circuitry. As system size increases, cumulative wiring, bias networks, and thermal load significantly complicate scaling to thousands or millions of neurons. Therefore, although Josephson circuits provide high speed and energy efficiency, their intricate dynamics, sensitivity to fabrication tolerances, and stringent cryogenic requirements render them among the most technically demanding neuromorphic platforms currently under development.

In contrast, this work introduces a shunted superconducting filament biased near its critical current as a minimal and elegant integrate-and-fire superconducting neuron. Superconducting nanowires were previously shown to emulate biological neuron behavior in Ref. 6; however, in that implementation the firing threshold and recovery time were distributed across several coupled nonlinear subsystems, resulting in a hybrid electrothermal oscillator rather than a single-element neuron. Moreover, the demonstrated performance was limited to binary fire-or-not behavior, while the larger electronic neural network was simulated using the LTspice software package⁷. Here we focus on the functionality of a single superconducting filament acting as a neuron and on integrating its temporal response into a neuromorphic circuit where the synaptic component can also consist of superconducting filaments with electronically controlled synaptic weights. Experimentally, we employ micrometer-scale superconducting wires as robust, controllable, and thermally stable neurons capable of reliable high-rate firing and seamless integration with other superconducting circuitry. Although nanowires offer advantages in miniaturization and reduced power consumption, they remain more susceptible to instability, thermal noise, and fabrication sensitivity, limiting their suitability for complex neuromorphic architectures with current technology. Nevertheless, the

concepts and neuromorphic strategies presented here are applicable to both nano- and micro-scale implementations.

Neural properties of a superconducting wirelet

A biological neuron exhibits a collection of characteristic behaviors^{6,8,9} that any artificial analogue must faithfully emulate. Here we characterize a shunted superconducting wirelet as a neural element and explain how it reproduces the essential biological features expected from a neuron.

The first fundamental property is the *threshold response*, namely the existence of a minimum input intensity below which the neuron does not fire. The calculated current-voltage (I-V) characteristic of a shunted superconducting wire shown in Fig. 1a clearly demonstrates this behavior. The intensity threshold corresponds to the critical current I_c , which separates the dissipationless superconducting state from the resistive state. Once the applied current exceeds I_c , voltage spikes emerge due to the periodic formation of hot spots¹⁰⁻¹² (see insets of Fig. 1b), accompanied by current diversion into the shunt resistor and resulting in measurable voltage pulses.

Biological neurons also exhibit a *refractory period*, meaning they can respond to consecutive input stimuli only if the time interval between them exceeds a characteristic recovery time. In our system, this timescale is governed by the delay time¹³, defined as the time required for an applied current above I_c to destabilize the superconducting state and generate a hot spot. Because the delay time decreases with increasing applied current, the refractory period is intrinsically current dependent. The simulated $V(t)$ curves in Fig. 1b further show that the firing frequency increases

with input current amplitude, corresponding to *class-I neuronal behavior*.

Finally, the shunted superconducting wirelet can reproduce neuronal death, defined as the loss of firing capability. As shown in Fig. 1c-d, sufficiently large applied currents suppress voltage spikes entirely. Simulations reveal that the system reaches a dynamical equilibrium characterized by stabilization of a phase-slip line¹⁴⁻¹⁶ (see insets of Fig. 1d and Supplementary Video 1), where current redistribution between the superconducting channel and the shunt no longer varies in time. This regime corresponds to the neuronal ‘dead mode’¹⁷ and has not previously been discussed for shunted superconducting nanowire elements.

Experimental realization of a spiking neuron

For the experimental realization of a superconducting neuron, we used 20 nm thin NbTiN whiskers measuring $3\mu\text{m}$ in width. A metallic resistor was mounted in parallel with the superconducting wire, with resistance values between 0.3 and 2Ω . The filaments were biased with a current pulse of 450 ns duration in the transport setup shown in Fig. 2a. Measurements were performed in a closed-cycle cryostat to maintain a stable temperature between 5 and 8 K, for a critical temperature of approximately 10 K. Further experimental details are provided in the Methods section.

Figure 2b presents the measured temporal evolution of the voltage along the wirelet shunted by 1Ω , for an applied current slightly exceeding the critical current I_c at 8 K. As predicted theoretically, the delay time decreases and the spiking frequency increases as the bias current rises, reflecting the enhanced rate of hot-spot formation and recovery in the resistive regime. This tun-

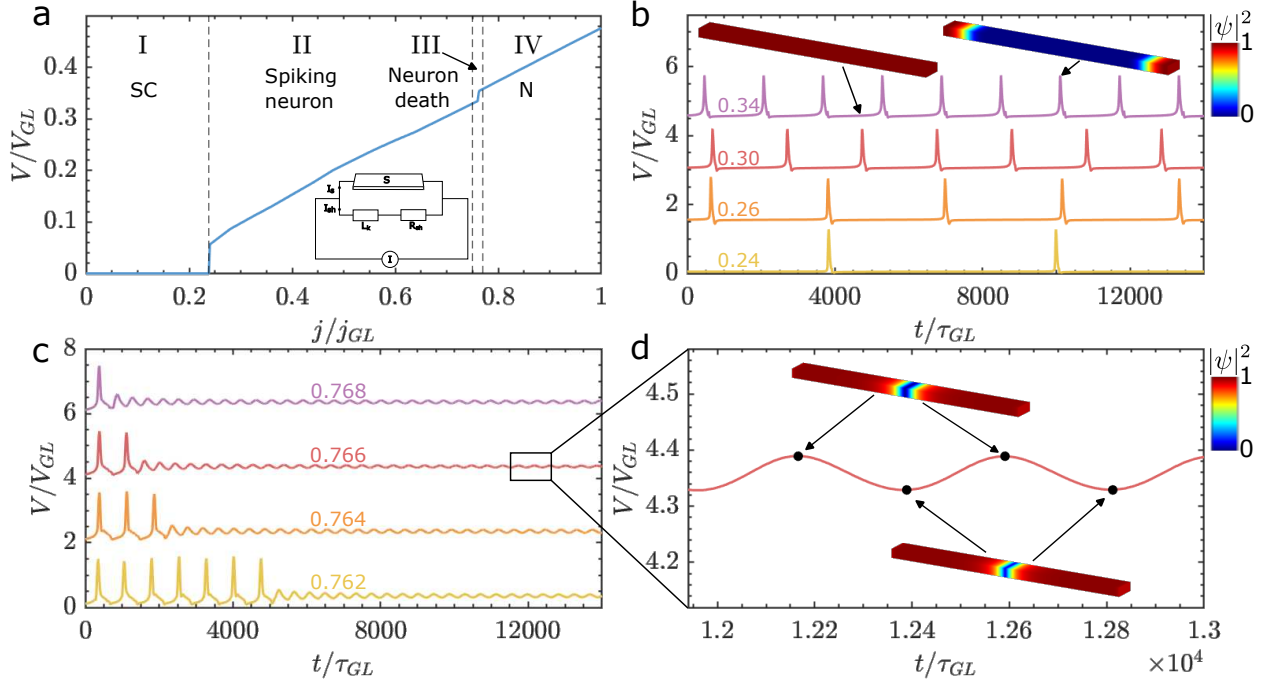


Figure 1: Simulation insight into the resistive state of a shunted superconducting filament. a, The calculated current-voltage characteristics of a shunted nanowire (width 10ξ , schematic circuit in inset, with $L_k = 500L_{GL}$ and $R_{sh} = 0.5R_{GL}$; see details in Methods), with four main phases labeled. **b,** The spiking temporal behavior of the output voltage, for increased applied current (shown on each curve, in units of j_{GL}) within phase II. $V(t)$ curves are vertically displaced for visibility. Insets show the snapshot of the superconducting condensate in the filament before and during the voltage spike. **c,** Temporal behavior of the output voltage within phase III, showing the transformation of spiking behavior into damped oscillations corresponding to the continuous phase-slip state. **d,** Zoom-in on the phase-slip state from panel c), with visualization of its Cooper-pair density profile.

ability of oscillation frequency via bias current provides a natural control parameter for neuron-like operation, analogous to firing-rate modulation in biological neurons. By adjusting the bias level, the spike rate, amplitude, and temporal regularity can be varied continuously, enabling analog information encoding in the spiking frequency. Such current-controlled frequency modulation therefore offers a convenient mechanism for input processing and electronic adaptation of the neuron response to the applied current. However, when the applied current exceeds the onset of phase III in Fig. 1a (at I_d), the spiking oscillations gradually give way to the phase-slip state, as shown in Fig. 2c. This transition represents an effective death of the superconducting wirelet neuron in experiment, consistent with theoretical predictions (Fig. 1c,d).

For this realization of the neuron, defined by the chosen material and wirelet dimensions, Figure 3 summarizes the measured spiking characteristics across accessible parameters. Panels (a) and (b) show spiking frequency versus bias current for various temperatures and shunt resistances. Oscillation frequencies span 4–40 MHz for currents between 0.5 and 5 mA. The temperature dependence reflects the interplay between thermal relaxation and critical current modulation, while shunt resistance variations demonstrate how electrodynamic coupling and energy dissipation determine oscillatory stability. The temperature–current phase diagram in Fig. 3c maps operational regimes for a 1Ω shunt, identifying the active spiking region between the superconducting and normal states, demonstrating a robust window for neuromorphic integration.

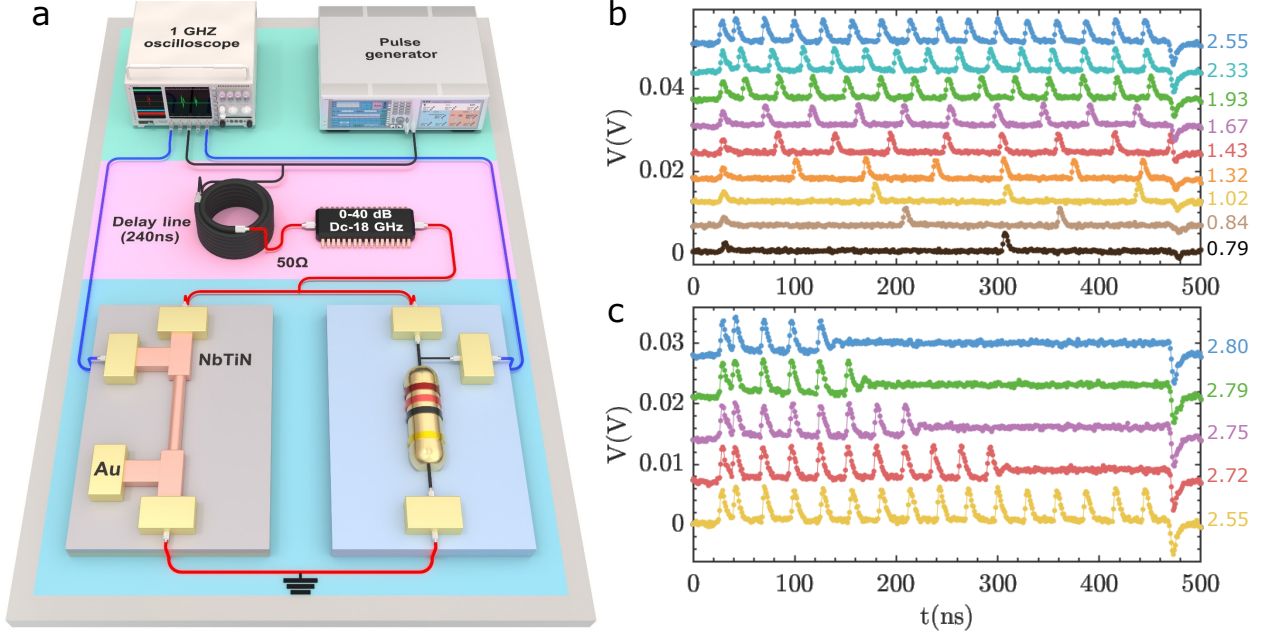


Figure 2: Experimental characterization of a spiking superconducting filament. Transport measurement on a $3\mu\text{m}$ -wide NbTiN filament shunted by 1Ω resistor, at $T = 8\text{K}$. **a**, The experimental setup. **b**, The measured spiking behavior of the voltage, for increasing applied current (shown in mA). Curves are vertically displaced for visibility. **c**, The death of the superconducting neuron, corresponding to Fig. 1c,d. The behavior seen in panels b,c has been validated at different temperatures, as shown in the Extended Data Fig. 1.

Pattern recognition with few superconducting neurons

To demonstrate the integration of individual superconducting wirelets into a functional neuromorphic hardware element, we implement a minimal neural network composed of three superconducting neurons, tasked with recognizing digits (0–9) from 3×3 -pixel digital images, as illustrated in Fig. 4a. Although the architecture contains only three neurons, the task is deliberately made non-trivial by introducing graded pixel brightness, thereby increasing the analog complexity of the

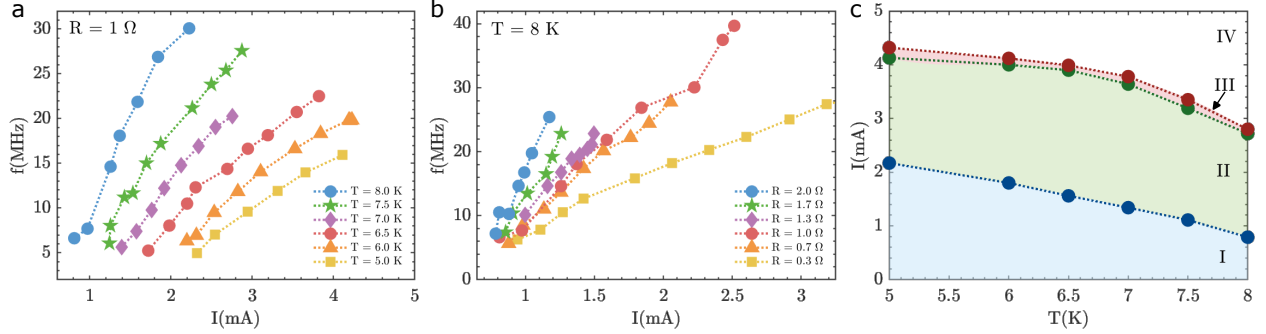


Figure 3: Control of spiking frequency. **a**, Spiking frequency of the superconducting filament from Fig. 2, increasing with applied current, for different temperatures. **b**, Spiking frequency of the same filament, as a function of applied current, at temperature $T = 8$ K, but for varied shunt resistance. The spiking behavior has been validated for all used shunt resistances, as shown in Extended Data Fig. 2. **c**, The full temperature-current phase diagram of the superconducting neuron from Fig. 2. Phase II is the operational range of the neuron.

input patterns. With the maximum brightness normalized to unity, bright pixels take intensity values of 0.8, 0.9, and 1.0, while dark pixels correspond to 0.0, 0.1, and 0.2, enabling subtle contrast variations within each digit representation. Each pixel intensity is converted into a current pulse whose amplitude is proportional to its brightness, encoding visual information in both temporal and amplitude domains. These pulses are sequentially applied, from the top-left to the bottom-right pixel, to the three superconducting neurons, which process the input stream in real time and generate voltage responses characteristic of the input pattern. The same pulse train with identical current amplitudes is delivered to all three neurons; therefore, the pixel intensity range is mapped to a current interval bounded by the maximal I_c and minimal I_d among the neurons.

The same pattern-recognition problem was solved using both theoretical simulations and

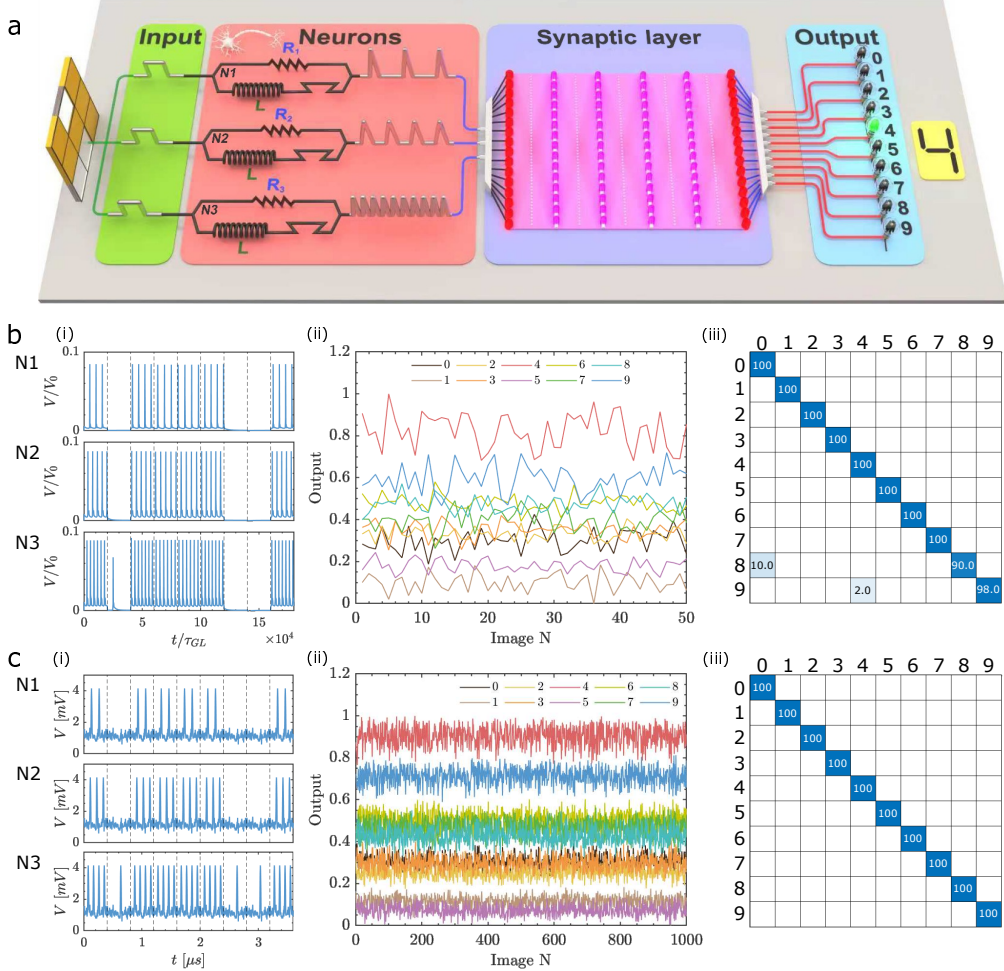


Figure 4: Proof-of-concept pattern recognition with three superconducting neurons. **a**, Schematic diagram of the circuit, where synaptic multiplexing was software-based. **b**, Simulated performance of three identical filaments (width 10ξ , and shunt resistances $0.5, 0.75$, and $1R_{GL}$) in a neural network: (i) exemplified output voltages of each neuron corresponding to the same train of input current pulses for pixels 1-9. (ii) Output result after training, for 50 different images of digit 4. (iii) The input-output matrix for 50 test images of each digit, with percentages of correct and erroneous predictions shown. **c**, Three experimental NbTiN filaments as in Fig. 2 (width $3\mu\text{m}$, and shunt resistances $0.3, 1$, and 1.7Ω top to bottom) in a neural network: (i) exemplified output voltages of each neuron corresponding to the same train of input current pulses for pixels 1-9. (ii) Output result after training, for 1000 different test images of digit 4. (iii) The input-output prediction matrix for 1000 test images of each digit, showing 100% accuracy.

experimental data for cross-validation. The theoretical results are shown in Fig. 4b. Panel **b(i)** presents the calculated voltage response of each neuron, with shunt resistance increasing from top to bottom, for the representative example of digit 4. Black dashed lines indicate the time windows corresponding to the current pulses associated with each pixel (see Supplementary Video 2 for the order parameter dynamics). The voltage traces of the three neurons are combined into an array $V(t) = [V_1(t), V_2(t), V_3(t)]$. During synaptic processing (see Methods), this array is linearly transformed using the cross-entropy loss method¹⁸ to generate a 1×10 probability vector whose elements represent the likelihood that the input image corresponds to digits 0–9. An example of this probability distribution is shown in panel **b(ii)** for digit 4. The predicted output of the network is defined as the digit associated with the maximum probability value.

In the simulations, the linear transformation was trained on a dataset of 250 images per digit. The trained network was subsequently tested on 50 previously unseen images per digit. The results, summarized in panel **b(iii)**, demonstrate 100% prediction accuracy for digits 0–7, 90% for digit 8, and 98% for digit 9. For the experimentally realized network, the corresponding results are presented in Fig. 4c. The identical training and testing procedure was followed, but both datasets were expanded to 1000 images per digit to improve statistical robustness. As shown in panel **c(iii)**, this implementation achieved 100% prediction accuracy for all evaluated input images.

To further evaluate scalability and generalization capability, the task complexity was increased from simple 3×3 patterns to handwritten digits with resolution 22×20 pixels taken from the MNIST database¹⁹. Each pixel was again encoded as a current pulse and sequentially applied

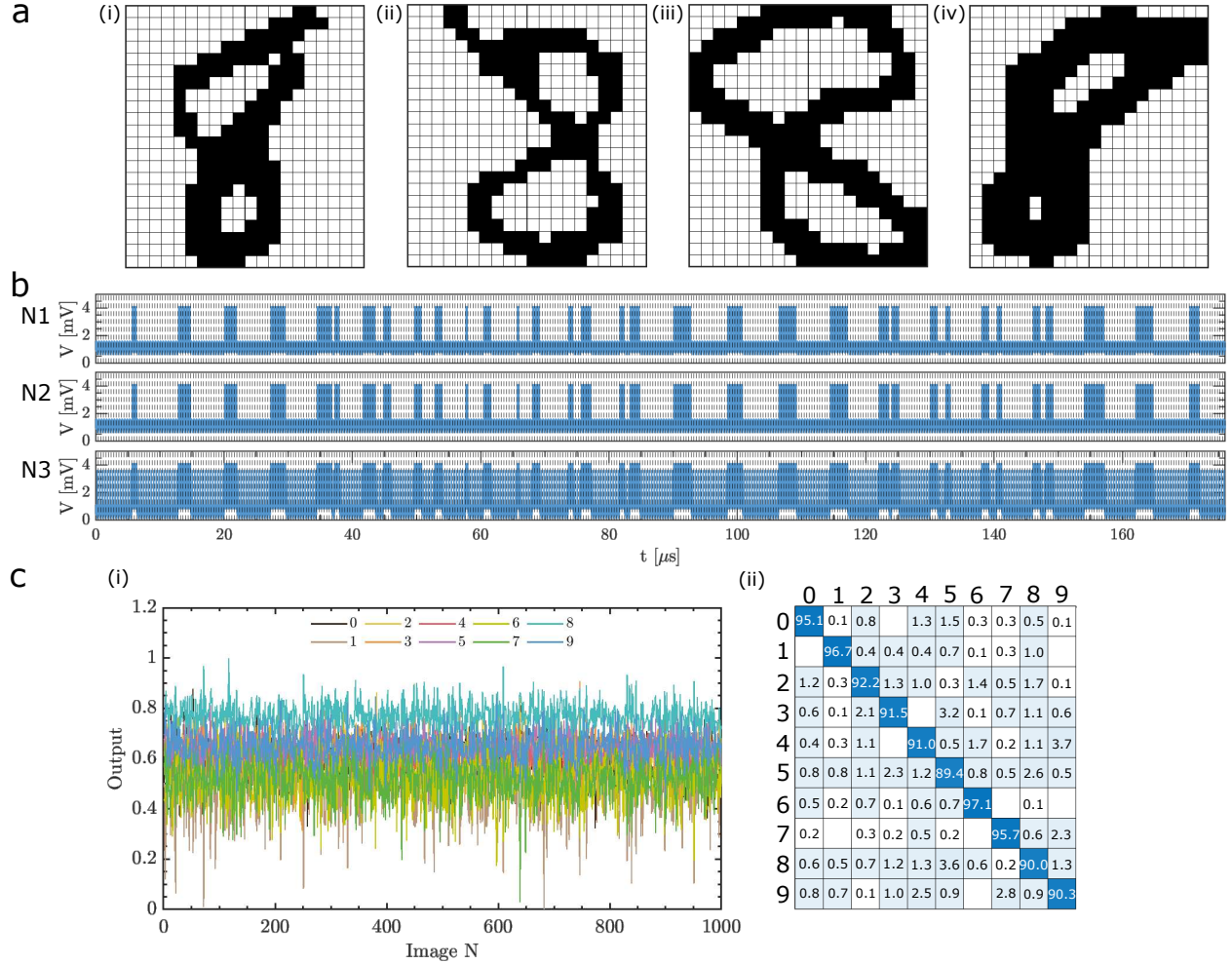


Figure 5: A complex task realized with same three-neuron network. **a, Illustrative examples of hand-written number 8 from the MNIST database. **b**, The temporal voltage output of the three neurons for the input sequence of 420 image pixels of the image a(i). **c**, Output result after synaptic processing of 1000 test images of digit 8. **d**, The full input-output matrix on 1000 test images of each digit, demonstrating 92.9% accuracy on average.**

to the same three superconducting neurons, preserving the circuit architecture used in the simpler classification task. Despite the substantial increase in input dimensionality and pattern variability, the system was successfully trained on 3000 images per digit and tested on 1000 unseen examples, as shown in Fig. 5. The resulting average prediction accuracy reached 92.9%, demonstrating that even a compact three-neuron superconducting wirelet network can extract and classify complex spatial patterns (see Supplementary Video 3 for the evolution of accuracy during training). From the perspective of neural network theory, this performance highlights the strong nonlinear feature mapping intrinsic to superconducting neurons. According to established scaling principles in deep learning^{18,20,21}, increasing the number of input neurons is expected to further enhance classification accuracy beyond conventional digital neural systems. These findings confirm the scalability and promise of superconducting neuromorphic circuits for high-speed, low-power pattern recognition at large data scales^{2,22}.

On-chip training with superconducting wirelet neurons In our results, synaptic training of the experimental neuron responses was performed using dedicated software. However, the circuitry depicted in Fig. 4a admits a direct extension that enables fully hardware-based on-chip training of the neural network. In this pattern-recognition architecture, an array of superconducting wirelet neurons, as many as required and distinctly shunted, receives a time-encoded chain of input current pulses representing the pixel intensities of an image. The voltage spikes generated by all input neurons are then combined sequentially in time to form a single aggregate output waveform. This waveform is subsequently converted into a current pulse and distributed among multiple superconducting output wirelets, each corresponding to a possible classification outcome and not

necessarily identical to the input neurons.

In contrast to the input stage, the output wirelets are not shunted. Instead, they incorporate electrostatic gates that modulate their local critical current^{23,24}, thereby controlling the partitioning of the injected output current. Such electrostatic gating provides a robust and efficient mechanism for signal processing and synaptic training, enabling dynamic adaptation of the response without structural reconfiguration of the superconducting circuitry. Within this framework, the gate voltages function as trainable synaptic weights. Importantly, the gate voltage is time dependent, since its distributed weight must be optimized over the full temporal profile of the aggregated input waveform. This temporal weighting allows each segment of the waveform to contribute differently to the final decision variable.

By sequentially feeding the voltage responses of all input neurons and applying a time-dependent gating function, each output wirelet performs a real-time weighted summation of the complete input sequence. During training, the gate voltages are tuned such that the wirelet producing the largest output voltage corresponds to the correct classification result. For the digit-recognition task shown in Fig. 5, ten output wirelets are required, each associated with one digit from 0 to 9. This gated superconducting synaptic stage enables compact, energy-efficient, and reconfigurable functionality within a fully cryogenic computing platform. A central advantage of this architecture is the unification of training and inference: the same superconducting circuitry that generates the output response also allows direct electronic adjustment of synaptic weights *in situ*. All elements, including neurons, interconnects, and gated synapses, can be integrated on a single

superconducting chip, ensuring scalability, minimal parasitic losses, and seamless integration with established superconducting electronics and quantum-circuit technologies.

Discussion and conclusions

Energy efficiency In our superconducting wirelet neuron architecture, the total energy associated with a spiking operation can be decomposed into three main contributions. The spike-generation energy, corresponding to the formation of a voltage pulse in the firing nanowire, is approximately 100 fJ. The subsequent voltage-to-current conversion stage dominates the energy budget, requiring about 1 pJ per spike to drive the output network. The resulting current is distributed among ten output wirelets, each functioning as a gated weighted synapse that converts the received current back into a voltage pulse, consuming up to 100 fJ per output event. When the total dynamic energy is averaged across the ten synaptic outputs, the effective system-level energy per synaptic event remains well below 0.5 pJ, positioning this platform among the most energy-efficient neuromorphic hardware implementations reported. For comparison, state-of-the-art digital neuromorphic processors such as ODIN²⁵ and Intel Loihi-2²⁶ demonstrate minimum energies of approximately 10–20 pJ per synaptic operation, while analog mixed-signal systems such as BrainScaleS-2²⁷ operate at similar magnitudes. Photonic neuromorphic platforms have achieved femtojoule-level pulse energies²⁸ and sub-picojoule synaptic energies²⁹, though typically with substantial hardware overhead including lasers and drivers. Our superconducting wirelet approach bridges the gap between ultra-low-energy but experimentally demanding photonic spiking schemes and scalable electronic implementations, offering sub-picojoule system-level synaptic event energy with intrinsic cryo-

genic compatibility. Moreover, both spike energy and operation energy can be further reduced, since the switching current scales with wirelet width and the critical current density of the superconducting material. The present devices employ 3 μm -wide NbTiN wirelets, leaving significant room for geometric scaling and material optimization, potentially pushing efficiencies into the deep-femtojoule regime.

μ -neuron vs. nano-neuron Although the wirelet-based neuron concept does not fundamentally depend on wire size, the choice between micrometer- and nanometer-scale wires strongly influences performance and reliability. Micrometer-wide wires, as used in our experiments, provide enhanced thermal robustness, signal strength, and operational stability, enabling reproducible spiking behavior. Their larger cross-section supports higher critical currents and more efficient heat dissipation, reducing susceptibility to quenching and thermal noise during high-frequency operation^{30,31}. The increased volume also strengthens vortex pinning, yielding more predictable electrical responses in stray magnetic fields³². These features ensure robust and biologically faithful spiking dynamics essential for system-level reliability. Nanowires offer advantages in density and reduced operating energy, enabling compact interconnects and lower switching energies, but at the expense of thermal stability and greater fabrication complexity². Thus, while nanowires remain promising for ultra-compact architectures, micrometer-scale implementations currently provide a more balanced and reliable platform, while still allowing future improvements through controlled downscaling.

In summary, we have established shunted superconducting wirelets as a minimal yet fully

functional artificial neuron platform capable of bias-tunable spike generation. By exploiting the temporal voltage waveform in response to sequences of input current pulses, we demonstrated handwritten digit recognition with only three neurons, achieving high classification fidelity with drastically reduced architectural complexity. This neural network implementation also enables full on-chip learning, in which the synaptic training is performed on gated output wirelets, such that the synaptic and output layers are integrated. Such design eliminates the need for a separate complex synaptic network and achieves learning and inference within the same hardware layer. Altogether, this concept outlines a scalable route toward ultralow-energy neuromorphic hardware readily integrable with emerging superconducting and quantum technologies, and marks a frontier in superconducting artificial intelligence, where architectural simplicity meets high efficiency and functionality.

Methods

Experimental setup The experimental configuration followed and extended methodologies used in prior studies of current-biased superconducting nanowires under pulsed excitation³³, while adapted here for the micrometer-scale NbTiN wirelets and external tunable shunts.

Thin NbTiN superconducting whiskers, 20 nm thick and 3 μ m wide, were fabricated on sapphire and SiO₂/Si substrates at STARcryoelectronics (New Mexico, USA). Deposition was carried out under ultra-high-vacuum conditions to ensure optimal film uniformity and low defect density. The patterning of the superconducting filaments and the definition of gold electrical contacts were performed using optical photolithography followed by reactive ion etching and argon ion milling

to achieve clean superconducting edges and reliable electrical interfaces. The final device layout, shown schematically in Fig. 2a, features a central superconducting stripe approximately 800 μm long, connected at both ends to gold pads for electrical access.

To investigate the spiking characteristics of the superconducting wirelets, each device was connected in parallel with an external metallic resistor mounted off-chip. The shunt resistor values ranged from 0.3 Ω to 2.0 Ω (specifically 0.3, 0.7, 1.0, 1.3, 1.7, and 2.0 Ω), allowing systematic control of the current redistribution and damping. One end of the superconducting stripe was connected to a voltage-pulse source, while the opposite end was grounded together with the shunt resistor. This arrangement provided a simple yet effective test platform for studying the interplay between shunting and superconducting spiking dynamics. To verify that the observed spiking behavior was not specific to a particular device geometry, additional samples with stripe widths of 5 μm and 10 μm were fabricated and tested under identical experimental conditions. The characteristic spiking dynamics and delay-time dependencies were consistently reproduced across all wire widths, confirming the robustness and generality of the observed phenomena.

All measurements were performed in a vacuum environment within a closed-cycle cryostat, enabling stable temperature control above 5 K. The NbTiN whiskers exhibited a superconducting transition temperature (T_c) of approximately 10 K, consistent with high-quality films of similar stoichiometry.

Voltage pulses of 450 ns duration and 10 kHz repetition rate were applied to the devices, with pulse amplitude varied to explore operation above and below the critical current. The waveform

was delivered through an air-delay transmission line with a propagation delay of 240 ns, ensuring well-timed and reproducible excitation conditions. Owing to the $50\ \Omega$ coaxial cable impedance, the experimental configuration operated in an effectively current-biased regime.

The temporal voltage response was measured simultaneously across both the superconducting wire and the parallel metallic shunt using a high-speed digital oscilloscope with sub-nanosecond temporal resolution and $50\ \Omega$ input termination. Each dataset consisted of time-domain traces averaged over multiple pulse cycles to minimize noise and improve signal-to-noise ratio. The measured voltage–time profiles were then analyzed to extract spiking delay times, frequency responses, and the dependence on applied current and temperature, as discussed in the main text.

Time-dependent Ginzburg-Landau simulations The numerical modeling of each shunted superconductor was done by solving the time-dependent Ginzburg-Landau equation:

$$\frac{u}{\sqrt{1 + \gamma^2|\psi|^2}} \left(\frac{\partial}{\partial t} + i\varphi + \frac{\gamma^2}{2} \frac{\partial|\psi|^2}{\partial t^2} \right) \psi = (\nabla - i\mathbf{A})^2 \psi + \psi(1 - |\psi|^2), \quad (1)$$

where the order parameter ψ is scaled to its value in absence of magnetic field ψ_0 ; all lengths are expressed in units of the superconducting coherence length ξ ; field and vector potential are in units of H_{c2} and $H_{c2}\xi$, respectively, with H_{c2} being the bulk upper critical field $\Phi_0/2\pi\xi^2$; time is in units of $t_{GL} = \pi\hbar/8uk_B T_c$, with $u = 5.79$ being a constant coming from microscopic theory. The parameter γ is the product of inelastic electron-phonon scattering time and the GL gap at $T = 0$, Δ_{GL} . Without loss of generality, we used $\gamma = 10$ in our calculations. Finally, the scalar potential φ is given in units of $V_{GL}\hbar/2et_{GL}$. At each time step, the scalar potential is obtained by solving

the Poisson equation:

$$\nabla^2 \varphi = \nabla (\text{Im} [\bar{\psi}(\nabla - i\mathbf{A})\psi]). \quad (2)$$

Eqs. 1-2 are then numerically solved (see Ref. 34 for details on the discretization), using a grid size $\Delta x = \Delta y = 0.2\xi$. The current density J_s transported by the superconducting wirelet of size $L \times w$ is introduced through the boundary conditions for the scalar potential as $\nabla \varphi(\pm L/2, y) = J_s \hat{x}$. At the remaining boundaries of the wirelet we have $\nabla \varphi(x, \pm w/2) = 0$. For the order parameter, we have $\psi(\pm L/2, y) = 0$ at the current leads, and $(\nabla - i\mathbf{A})\psi|_y = 0$ at $y = \pm w/2$, assuring no supercurrent flows out of the sample on those boundaries.

To incorporate the effects of the shunt, we simultaneously solved for the time evolution of the transport current density in a shunted electrical system (see inset of Fig. 1a), from equation

$$L_K \frac{dJ_s}{dt} = (J - J_s)R_{sh} - V, \quad (3)$$

where J is the total current density applied to the circuit; L_K is the circuit kinetic inductance in units of $L_{GL} = (\Phi_0 e^* \pi / 8k_b u) / (\sigma_n \xi T_c)$, with σ_n being the normal state conductivity of the superconductor material; R_s is the shunt resistance, in units of $R_{GL} = 1 / (\sigma_n \xi)$; and V is the voltage drop across the superconducting wire. At each time step, Eq. 3 is solved and the current density J_s carried by the superconductor is recalculated.

Synaptic training The training of the neural network, realized in the synaptic layer of the circuit, was carried out using a dedicated control routine made into a custom-tailored software. In this process, the time-dependent voltage output of each of the three neurons $V_i(t)$ was discretized in

N steps equidistant in time, such that the cumulative waveform vector of those discretized arrays $\mathcal{V} = [V_1^d, V_2^d, V_3^d]$ has $3N$ elements. For the 3×3 images discussed in Fig. 4, we had $N = 1000$ for the training using numerical simulation results and $N = 1278$ for the training using experimental results. When working with the MNIST database, N was set to 62480.

The output of the network, a 10-element array y (one element for each possible digit) was then obtained by a linear transformation of \mathcal{V} :

$$y = \mathcal{V}W \quad (4)$$

where the weights are contained in the $3N \times 10$ matrix W . The targets T are then one-hot vectors with 10 elements.

For each epoch n_{eph} of the training process, we compute the output activations using a *softmax* function:

$$s = \frac{\exp(y)}{\sum_{i=1}^{10} \exp(y_i)}. \quad (5)$$

The cross-entropy loss function was then employed to quantify the prediction error between the network output and the target label:

$$L_{n_{eph}} = - \sum_{i=1}^{10} T \cdot \log(s). \quad (6)$$

Analytically, one can define the gradient of the cross-entropy loss with respect to the weights as:

$$G = \mathcal{V}^T (s - T). \quad (7)$$

The weight matrix parameters were updated via stochastic gradient descent (SGD) according to:

$$W = W - \eta G, \quad (8)$$

with $\eta = 0.01$ being the learning rate. The same procedure was reiterated through successive training epochs, allowing progressive adjustment of the synaptic weights until the network reached convergence.

1. Goswami, S., Hazra, D., Patra, B. & Das, A. Superconducting optoelectronic neurons for neuromorphic computing. *Journal of Applied Physics* **128**, 050902 (2020).
2. Shainline, J. M., Buckley, S. M., Mirin, R. P. & Nam, S. W. Superconducting optoelectronic circuits for neuromorphic computing. *Physical Review Applied* **12**, 034022 (2019).
3. Segall, K., Toomey, E., Basaran, A. & Berggren, K. K. Synchronization and control of superconducting nanowire neurons. *Physical Review E* **100**, 062408 (2019).
4. Shainline, J. M., Buckley, S. M., Mirin, R. P. & Nam, S. W. Superconducting optoelectronic neurons i: General principles. *Journal of Applied Physics* **124**, 152130 (2018).
5. Carnevale, G., Suri, B., Gol'tsman, G. N. & Rybin, D. S. Superconducting neurons for large-scale neuromorphic networks. *Superconductor Science and Technology* **34**, 094001 (2021).
6. Toomey, E., Berggren, K. K. & Segall, K. Operation of a superconducting nanowire as a spiking neuron. *Physical Review Applied* **11**, 034056 (2019).
7. Analog Devices, Inc. Ltspice (2023). URL <https://www.analog.com/ltspice>. Linear Circuit Simulation Software.
8. Izhikevich, E. M. Which model to use for cortical spiking neurons? *IEEE transactions on neural networks* **15**, 1063–1070 (2004).

9. Crotty, P., Segall, K. & Schult, D. Biologically realistic behaviors from a superconducting neuron model. *IEEE Transactions on Applied Superconductivity* **33**, 1–6 (2023).
10. Skocpol, W. J., Beasley, M. R. & Tinkham, M. Self-heating hotspots in superconducting thin-film microbridges. *Journal of Applied Physics* **45**, 4054–4066 (1974).
11. Kerman, A. J., Yang, J. K. W., Molnar, R. J., Dauler, E. A. & Berggren, K. K. Electrothermal feedback in superconducting nanowire single-photon detectors. *Physical Review B* **79**, 100509 (2009).
12. Zotova, A. N. & Vodolazov, D. Y. Hotspot formation and relaxation in current-carrying superconducting films. *Physical Review B* **85**, 024509 (2012).
13. Harrabi, K., Mekki, A. & Milošević, M. V. Characteristic times for gap relaxation and heat escape in nanothin nbtif superconducting filaments: thickness dependence and effect of substrate. *Nanomaterials* **14**, 1585 (2024).
14. Langer, J. S. & Ambegaokar, V. Intrinsic resistive transition in narrow superconducting channels. *Physical Review* **164**, 498–510 (1967).
15. McCumber, D. E. & Halperin, B. I. Time scale of intrinsic resistive fluctuations in thin superconducting wires. *Physical Review B* **1**, 1054–1070 (1970).
16. Arutyunov, K. Y., Golubev, D. S. & Zaikin, A. D. Superconductivity in one dimension. *Physics Reports* **464**, 1–70 (2008).

17. Schegolev, A. E., Klenov, N. V., Gubochkin, G. I., Kupriyanov, M. Y. & Soloviev, I. I. Bio-inspired design of superconducting spiking neuron and synapse. *Nanomaterials* **13**, 2101 (2023).
18. Goodfellow, I., Bengio, Y. & Courville, A. *Deep Learning* (MIT Press, 2016). URL <https://www.deeplearningbook.org>.
19. LeCun, Y., Bottou, L., Bengio, Y. & Haffner, P. Gradient-based learning applied to document recognition. In *Proceedings of the IEEE*, vol. 86, 2278–2324 (1998).
20. LeCun, Y., Bengio, Y. & Hinton, G. Deep learning. *Nature* **521**, 436–444 (2015).
21. Hestness, J. *et al.* Deep learning scaling is predictable, empirically. *arXiv preprint arXiv:1712.00409* (2017). URL <https://arxiv.org/abs/1712.00409>.
22. Chaudhary, K. *et al.* Superconducting optoelectronic hardware for neuromorphic computing. *Nature Electronics* **6**, 686–698 (2023).
23. De Simoni, G., Paolucci, F., Solinas, P., Strambini, E. & Giazotto, F. Metallic supercurrent field-effect transistor. *Nature Nanotechnology* **15**, 801–806 (2020).
24. Paolucci, F. *et al.* Field-effect control of metallic superconducting channels. *Physical Review Applied* **13**, 024061 (2020).
25. Frenkel, C., Lefebvre, M., Legat, J.-D. & Bol, D. A 0.086-mm² 12.7-pj/sop 64k-synapse 256-neuron online-learning digital spiking neuromorphic processor in 28-nm cmos. *IEEE Transactions on Biomedical Circuits and Systems* **13**, 145–158 (2019).

26. Davies, M. *et al.* Advancing neuromorphic computing with loihi: A survey of results and outlook. *Proceedings of the IEEE* **109**, 911–934 (2021).
27. Pehle, C. *et al.* The brainscales-2 accelerated neuromorphic system with hybrid plasticity. *Frontiers in Neuroscience* **16**, 795876 (2022).
28. Lee, Y.-J., On, M. B., Xiao, X., Proietti, R. & Yoo, S. J. B. Photonic spiking neural networks with event-driven femtojoule optoelectronic neurons based on izhikevich-inspired model. *Optics Express* **30**, 19360–19389 (2022).
29. Zeng, Y. *et al.* Photonic spiking neural network based on dml and dfb-sa laser chip for pattern classification. *Optics Express* **33**, 12045–12058 (2025). Reported energy efficiency of 0.625 pJ/MAC, implying sub-pJ per synaptic event.
30. Zhou, Z., Toomey, E., Segall, K. & Berggren, K. K. Behavior of superconducting nanowire neurons with different geometries. *IEEE Transactions on Applied Superconductivity* **29**, 1–5 (2019).
31. Berggren, K. K., Toomey, E., Zhao, Q.-Y. & Segall, K. Superconducting nanowire devices for neuromorphic computing. *IEEE Transactions on Applied Superconductivity* **28**, 1–5 (2018).
32. Cheng, R., Berggren, K. K. & Zhao, Q.-Y. Flux dynamics in superconducting nanowires: Implications for neuromorphic circuits. *Applied Physics Letters* **111**, 122602 (2017).
33. Harrabi, K., Levenson-Falk, E. M., Simmonds, R. W. & Wellstood, F. C. Dynamics of superconducting josephson junctions under pulsed excitation. *Applied Physics Letters* **114**, 052601 (2019).

34. Milošević, M. & Geurts, R. The ginzburg–landau theory in application. *Physica C: Superconductivity* **470**, 791–795 (2010).

Acknowledgments K.H. gratefully acknowledges the support of the King Fahd University of Petroleum and Minerals, Saudi Arabia, under project ISP23212. L.R.C. and M.V.M. acknowledge support from the Research Foundation-Flanders (FWO-Vlaanderen).

Author contributions Conceptualization: M.V.M. Methodology: K.H., L.R.C. and M.V.M. Investigation: All authors. Visualization: K.H. and L.R.C. Funding acquisition, project administration and supervision: K.H. and M.V.M. Writing, review and editing: All authors.

Competing Interests The authors declare no competing interests.

Correspondence Correspondence and requests for materials should be addressed to Khalil Harrabi (email: harrabi@kfupm.edu.sa) and Milorad V. Milošević (email: milorad.milosevic@uantwerpen.be).

Extended Data

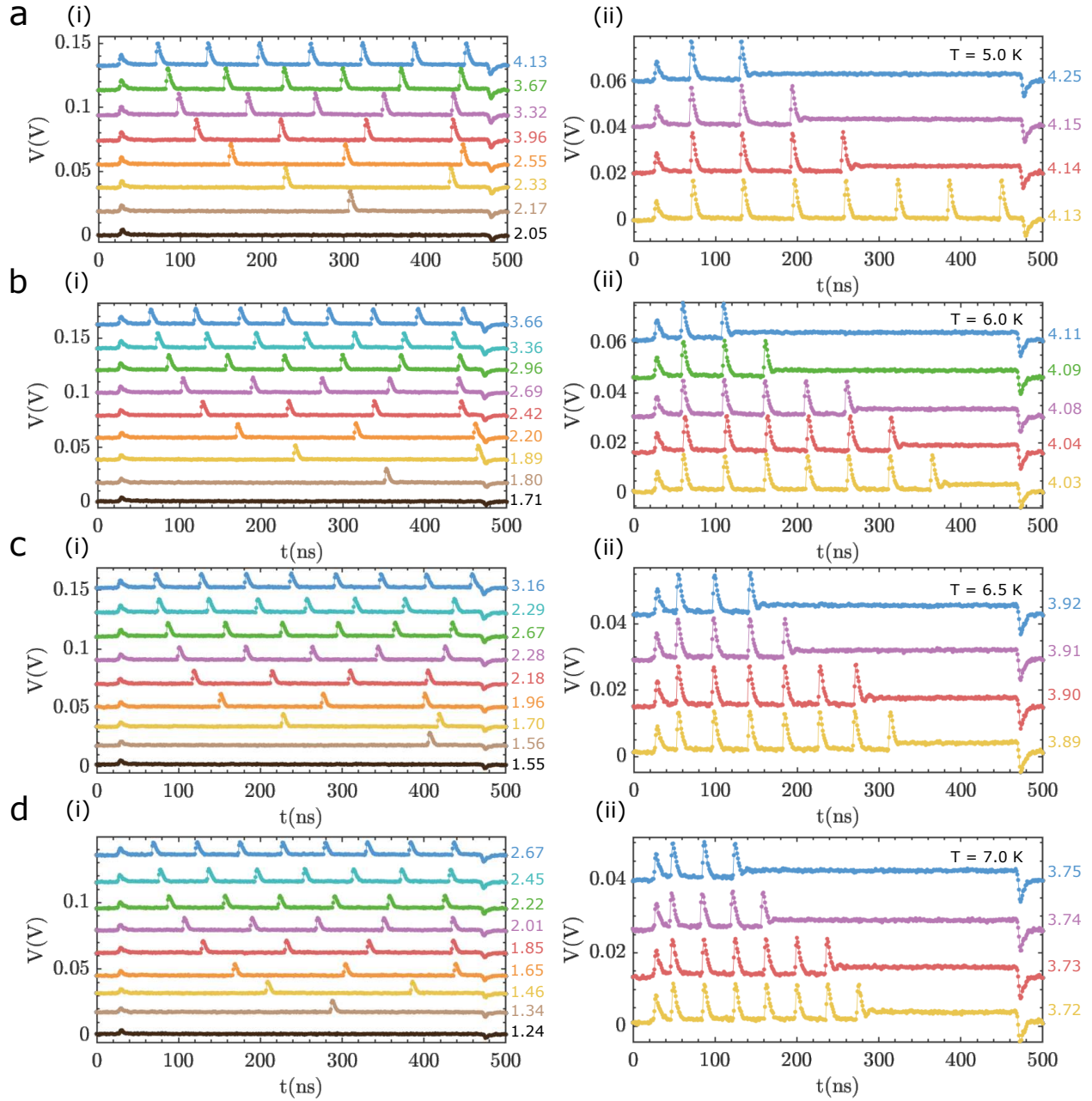


Figure ED1: Experimental characterization of a spiking superconducting filament at different temperatures. Transport measurement on a $3\mu\text{m}$ -wide NbTiN filament shunted by 1Ω resistor, analogous to Fig. 2b, and c, of the main text, but at different temperatures (indicated in the figure). Panels (i) and (ii) show the spiking behavior of the voltage and the death of the superconducting neuron. Currents are given in mA.

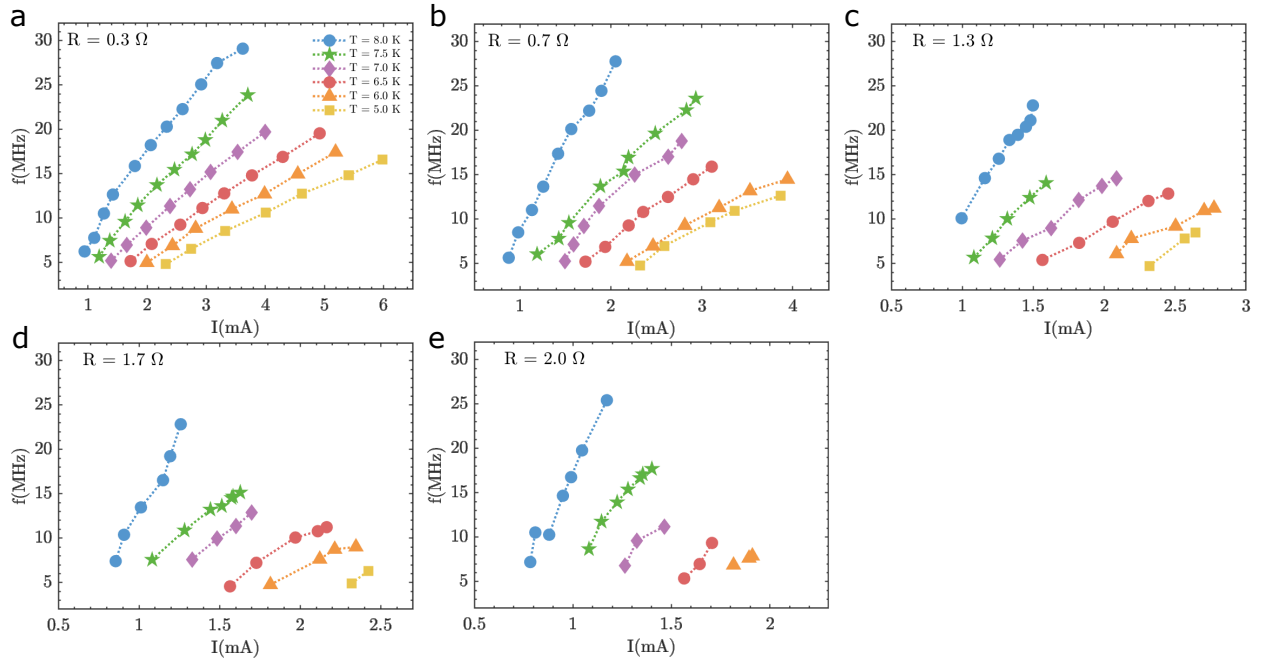


Figure ED2: Spiking frequency for different shunt resistance. The spiking frequency as a function of applied current at different temperatures. Shown panels are analogous to Fig. 3a of the main text, but correspond to different shunt resistances used, as indicated in the figure.